Check for updates

Mo-doped SnS₂ with enriched S-vacancies for highly efficient electrocatalytic N₂ reduction: the critical role of the Mo–Sn–Sn trimer†

Ke Chu, [iD] * Jing Wang, Ya-ping Liu, [iD] Qing-qing Li and Ya-li Guo

Vacancy engineering and heteroatom doping are two effective approaches to tailor the electronic structures of catalysts for improved electrocatalytic activity. Herein, these two approaches were rationally combined to modulate the structure of SnS_2 toward the N_2 reduction reaction (NRR) by means of Mo-doping, which simultaneously induced the generation of enriched S-vacancies (V_s). The developed Mo-doped SnS_2 nanosheets with enriched V_s presented a conspicuously enhanced NRR activity with an NH_3 yield of 41.3 µg h^{-1} mg^{-1} (-0.5 V) and a faradaic efficiency of 20.8% (-0.4 V) and are among the best SnS_2-based NRR catalysts to date. Mechanistic studies revealed that the co-presence of the Mo dopant and V_s enabled the creation of Mo–Sn–Sn trimer catalytic sites, capable of strongly activating N_2 even for the cleavage of the N≡N triple bond to the N=N double bond at the N_2 adsorption stage, consequently leading to a downhill process of the first hydrogenation step and a largely reduced energy barrier.

Dinitrogen (N_2) fixation to ammonia (NH_3) is an essential chemical process for the modern industrial society because NH_3 is a widely used feedstock for various chemical products and is also a promising carbon-free energy carrier.[1] The electrochemical N_2 reduction reaction (NRR) under ambient conditions holds great promise for green and sustainable NH_3 production,[2] in stark contrast to the industrial Haber–Bosch process which involves huge energy consumption and enormous CO_2 emission. However, the NRR process is largely limited by the unsatisfactory NH_3 production rate and low faradaic efficiency (FE), stemming from the extremely stable N≡N bond, poor N_2 adsorption/activation on the catalyst surface and the competing hydrogen evolution reaction (HER).[3] Exploring highly active electrocatalysts may hold the key to mitigating these limitations and realizing high NRR efficiency. Over the past three years, an increasingly large number of noble metals,[4–7] transition metal-based compounds,[8–14] and metal-free

School of Materials Science and Engineering, Lanzhou Jiaotong University, Lanzhou 730070, China. E-mail: chukelut@163.com

† Electronic supplementary information (ESI) available. See DOI: 10.1039/d0ta01688h

materials[15–19] have been designed as promising candidates toward the NRR.

SnS_2-based materials have shown great potential in electrolysis applications, owing to their fascinating catalytic performance, good stability, tunable electronic structures, and 2D morphology with largely exposed active edges.[20] Recently, SnS_2 has been proved to be an attractive catalyst with favorable NRR activity as well.[21,22] Nonetheless, the reported NRR performance of SnS_2 materials is still far from satisfactory and competitive with that of the state-of-the-art NRR catalysts. The main bottlenecks are the poor NRR activation, *i.e.*, the high energy barrier for the first hydrogenation step,[22] and the low intrinsic electrical conductivity, *i.e.*, the inefficient proton-coupled electron transfer process, even when employing approaches such as growth of amorphous Sn on crystalline SnS_2 nanosheets (FE: 6.5%)[21] and construction of well-aligned SnS_2 nanoarrays on porous Ni foam (FE: 11.2%).[22] Thus, more efficient methods are still needed to further enhance the intrinsic NRR activity of SnS_2.

As an effective strategy for electronic structure modulation of the catalysts, vacancy engineering by introducing anion vacancies into the catalyst lattice,[23] such as oxygen vacancies (TiO_2,[24] WO_3 (ref. 25) and MnO_2 (ref. 26)), and nitrogen vacancies (C_3N_4,[27] VN[28] and W_2N_3 (ref. 29)), provides unique active sites for the effective adsorption and activation of dinitrogen. In addition, heteroatom doping is another widely used method to optimize the adsorption of NRR intermediates on catalysts and promote the NRR reaction kinetics,[30–33] which have been demonstrated in V-doped TiO_2,[34] Fe-doped Ni_2P[35] and Mo-doped MnO_2.[36] More importantly, heteroatom doping has been recently confirmed to facilitate the generation of vacancies, while the synergistic effect of dopants and vacancies leads to a conspicuously enhanced NRR performance.[37,38] For instance, introducing Zr-dopants in TiO_2 nanotubes has been reported to favorably generate both enriched oxygen vacancies and bi-Ti^{3+} pairs,[38] and the bi-Ti^{3+} pairs serve as the dominant active sites in facilitating the catalytic performance of the NRR with an FE of 17.3%. Similar results and a more improved NRR

performance (FE: 25.6%) have been presented in Fe-doped TiO_2 nanoparticles,[37] where the combined effect of bi-Ti^{3+} pairs and oxygen vacancies contributes to the substantially boosted NRR activity. Inspired by these studies, it is anticipated that the NRR performance of SnS_2 may be greatly enhanced by the combination of vacancy engineering and heteroatom doping.

In this study, we rationally combined vacancy engineering and heteroatom doping to regulate the electronic structure of SnS_2 by Mo-doping, which enabled the spontaneous generation of enriched S-vacancies (V_s) as well. The developed Mo-doped SnS_2 nanosheets with enriched V_s exhibited a significantly enhanced NRR activity with an NH_3 yield of 41.3 μg h^{-1} mg^{-1} (−0.5 V) and an FE of 20.8% (−0.4 V) and were among the best SnS_2-based NRR catalysts to date. Density functional theory (DFT) calculations revealed that the co-presence of the Mo dopant and V_s enabled the creation of Mo–Sn–Sn trimer active sites that could strongly activate N_2 and lower the reaction energy barrier.

Mo-doped SnS_2 (Mo-SnS_2) nanosheets were directly grown on CC *via* a facile hydrothermal method. Pristine SnS_2/CC was also prepared as a reference. The synthesis details are provided in the ESI.† The obtained SnS_2 and Mo-SnS_2 nanosheets scraped from CC were first investigated by X-ray photoelectron spectroscopy (XPS). As shown in Fig. 1a, the deconvolution of the Mo3d spectrum results in three well-resolved peaks of S2s (226.4 eV), $Mo^{4+}3d_{3/2}$ (229.3 eV) and $Mo^{4+}3d_{1/2}$ (232.7 eV) for Mo-SnS_2 nanosheets, which are absent in pristine SnS_2 nanosheets, indicating the successful Mo-doping in the Mo-SnS_2 nanosheets. Fig. 1b shows the XRD patterns of SnS_2/CC and Mo-SnS_2/CC. Excluding the peaks of CC, both samples display a pure hexagonal SnS_2 phase (JCPDS no. 23-677) with no detectable impurities. Obviously, all the peaks of Mo-SnS_2/CC are much weaker than those of SnS_2/CC, indicating the lowered crystallinity of Mo-SnS_2 caused by Mo-doping. The morphologies of SnS_2 and Mo-SnS_2 nanosheets were further investigated by scanning electron microscopy (SEM), transmission electron microscopy (TEM) and high-resolution TEM (HRTEM). The SEM images show that bushy nanosheets are densely and vertically anchored on the CC for both SnS_2/CC (Fig. 1c) and Mo-SnS_2/CC (Fig. 1d). The nanosheet features can be further revealed by TEM with the observation of clear wrinkles and corrugations on SnS_2 (Fig. 1e) and Mo-SnS_2 (Fig. 1f) nanosheets.[39–41] The HRTEM image shows that the pristine SnS_2 nanosheets (Fig. 1g) possess a high crystallinity as evidenced by the sharp lattice fringes with a spacing value of 0.59 nm, assigned to the (001) facet of SnS_2. In contrast, blurred and discontinuous lattice fringes can be observed in Mo-SnS_2 nanosheets (Fig. 1h), indicating that Mo-doping can remarkably reduce the crystallinity of Mo-SnS_2 nanosheets, consistent with the XRD analysis (Fig. 1b). The selected areas in Fig. 1h (A and B squares), when applying an Inverse Fast Fourier Transform (IFFT) mask, display obvious distortions and dislocations in the lattice fringes,[42–44] suggesting the existence of plentiful defects (*i.e.*, vacancies) in Mo-SnS_2 nanosheets, which rationalizes the reduced crystallinity of Mo-SnS_2. The scanning TEM (STEM) elemental mapping images (Fig. 1i) reveal that considerable Mo dopants are uniformly distributed on the entire surface of Mo-SnS_2 nanosheets.

The vacancies existing in Mo-SnS_2 nanosheets were further investigated by a combination of XPS, electron paramagnetic resonance (EPR) spectroscopy and DFT analysis. For both SnS_2 and Mo-SnS_2 nanosheets, the XPS Sn3d spectra (Fig. 2a) reveal $Sn3d_{5/2}$ (∼486 eV) and $Sn3d_{3/2}$ (∼495 eV) states of Sn^{4+}, and the S2p spectra (Fig. 2b) reveal $S2p_{3/2}$ (∼161 eV) and $S2p_{1/2}$ (∼163 eV) states of S^{2-}. With respect to those of the pristine SnS_2 nanosheets, the Sn3d and S2p spectra of Mo-SnS_2 nanosheets are negatively shifted by 0.4 and 0.3 eV, respectively, suggesting the decreased valence state and increased electrons in Mo-SnS_2 nanosheets caused by the presence of V_s.[45] The existence of enriched V_s in Mo-SnS_2 nanosheets can also be directly verified from the remarkably reduced atomic ratio of S/Mo from 1.88 (SnS_2) to 1.62 (Mo-SnS_2) derived from the XPS element analysis. In the EPR spectra (Fig. 2c), the signal at $g = 2.001$ represents the electrons trapped in V_s. Compared to SnS_2 nanosheets, Mo-SnS_2 nanosheets exhibit a much stronger EPR signal intensity, suggesting a higher concentration of V_s,[23] consistent with the XPS results. To gain further insight, DFT was applied to predict the V_s formation energy (E_f). As shown in Fig. 2d, the formation of isolated V_s in SnS_2-V_s requires a largely positive E_f (5.25 eV) and thus is thermodynamically unfavorable. With the introduction of the Mo dopant (Fig. 2e), V_s can be favorably formed at the Mo-adjacent site of Mo-SnS_2-V_s with a significantly reduced E_f (−0.78 eV). Therefore, the DFT results concur well with the XPS/EPR measurements and demonstrate that Mo-doping can considerably lower the V_s formation energy and enable the spontaneous generation of V_s in Mo-SnS_2 nanosheets.

DFT calculations were used to further investigate the electronic structure of Mo-SnS_2-V_s. From the electron contour maps sliced along the (001) plane, it can be seen that more electrons are accumulated in the Mo/V_s region in Mo-SnS_2-V_s (Fig. 2g) as compared to SnS_2 (Fig. 2f), which is also confirmed by the differential charge density (Fig. S1†). Upon N_2 adsorption, it is believed that these Mo/V_s-induced abundant accumulated electrons can be easily transferred into the anti-bonding orbitals of N_2 molecules for the weakening and dissociation of the N≡N bond.[46] Projected density of states (PDOS, Fig. 2h) analysis indicates that SnS_2 possesses a 0.64 eV bandgap indicative of its semiconducting character. In contrast, the co-presence of the Mo-dopant and V_s creates noticeable electronic states crossing the Fermi level, leading to the metallic characteristics of Mo-SnS_2-V_s and thus higher conductivity relative to that of SnS_2, which is favorable for the proton-coupled electron-transfer process to boost the NRR kinetics. Meanwhile, the calculated work function (Fig. 2i & S2†) indicates that Mo-SnS_2-V_s (5.513 eV) possesses a lower work function than SnS_2 (6.758 eV), which suggests the higher capability of Mo-SnS_2-V_s for electron back-donation from its active sites to the absorbed N_2 and NRR intermediates,[47–49] thus facilitating N_2 adsorption, activation, and hydrogenation.

The electrocatalytic NRR performance of Mo-SnS_2/CC as a self-standing electrode was examined in N_2-saturated 0.5 M $LiClO_4$ using a gas-tight two-compartment cell, as displayed in Fig. S3.† An absorber was placed at the end of the cell to prevent the loss of produced NH_3 by N_2 flow during the NRR test.[50] All potentials were converted into values *versus* the reversible
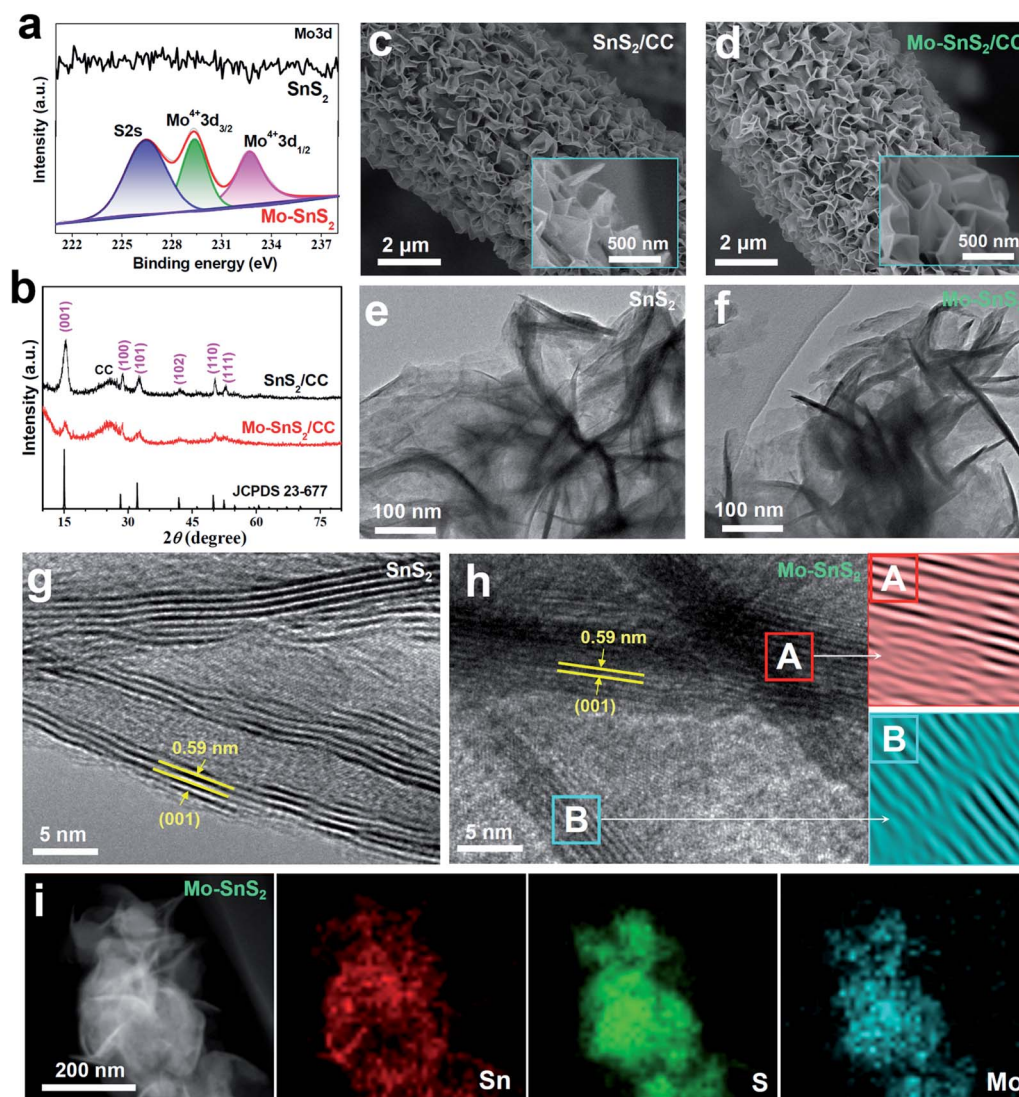
7118 | *J. Mater. Chem. A*, 2020, **8**, 7117–7124

This journal is © The Royal Society of Chemistry 2020

Fig. 1 (a) XPS Mo3d spectrum of SnS_2 and Mo-SnS_2 nanosheets scraped from CC. (b) XRD patterns for SnS_2/CC and Mo-SnS_2/CC. (c and d) SEM images of (c) SnS_2/CC and (d) Mo-SnS_2/CC. (e and f) TEM images of (e) SnS_2 and (f) Mo-SnS_2 nanosheets. (g and h) HRTEM images of (g) SnS_2 and (h) Mo-SnS_2 nanosheets (A and B are the corresponding IFFT images recorded from regions A and B in (h)). (i) STEM element mapping images for Mo-SnS_2 nanosheets.

hydrogen electrode (*vs.* RHE), and the standard RHE was experimentally calibrated using cyclic voltammetry curves in a high-purity hydrogen saturated solution (Fig. S4†).[36] The concentration of generated NH_3 was experimentally determined by the indophenol blue method,[51] while the concentration of the possible N_2H_4 as a byproduct was measured by the Watt–Chrisp approach.[52] Their standard calibration curves are shown in Fig. S5 and S6.† As displayed in Fig. S7,† N_2H_4 can hardly be detected, implying a high NRR selectivity for Mo-SnS_2/CC for N_2-to-NH_3 conversion.

The polarization curves recorded by linear sweep voltammetry (LSV, Fig. 3a) show a higher current density in N_2-saturated solution than in Ar-saturated solution, suggesting the feasibility of the NRR on Mo-SnS_2/CC. Before the quantitative evaluation of the NRR performance, a series of control tests were preliminarily carried out to exclude the possible influences

from any nitrogen contaminants.[53] The isotopic labeling measurements based on ^{1}H nuclear magnetic resonance (NMR) were first utilized to trace the origin of the N source, as shown in Fig. 3b. After NRR electrolysis using $^{14}N_2$ or $^{15}N_2$ as the feed gas, a triplet for $^{14}NH_4^+$ ($^1J_{N-H}$ = 52 Hz) or a doublet for $^{15}NH_4^+$ ($^1J_{N-H}$ = 72 Hz) can be distinguished, respectively, whereas no labeled $^{14}NH_4^+$ or $^{15}NH_4^+$ can be found when using Ar as the feed gas. In addition, UV-vis analysis (Fig. S8†) in an Ar-saturated solution, or at open circuit, or on pristine CC does not produce a detectable amount of NH_3.[54–56] Furthermore, the time-dependent test (Fig. S9†) shows that the produced NH_3 increases linearly with the electrolysis time, indicating that NH_3 can be continuously generated by NRR catalysis over Mo-SnS_2/CC. We also employed the ion chromatography (IC) technique to quantitatively determine the concentration of NRR-derived NH_3. As depicted in Fig. 3c and S10,† the IC measurement (1.27 μg mL^{-1}) is very
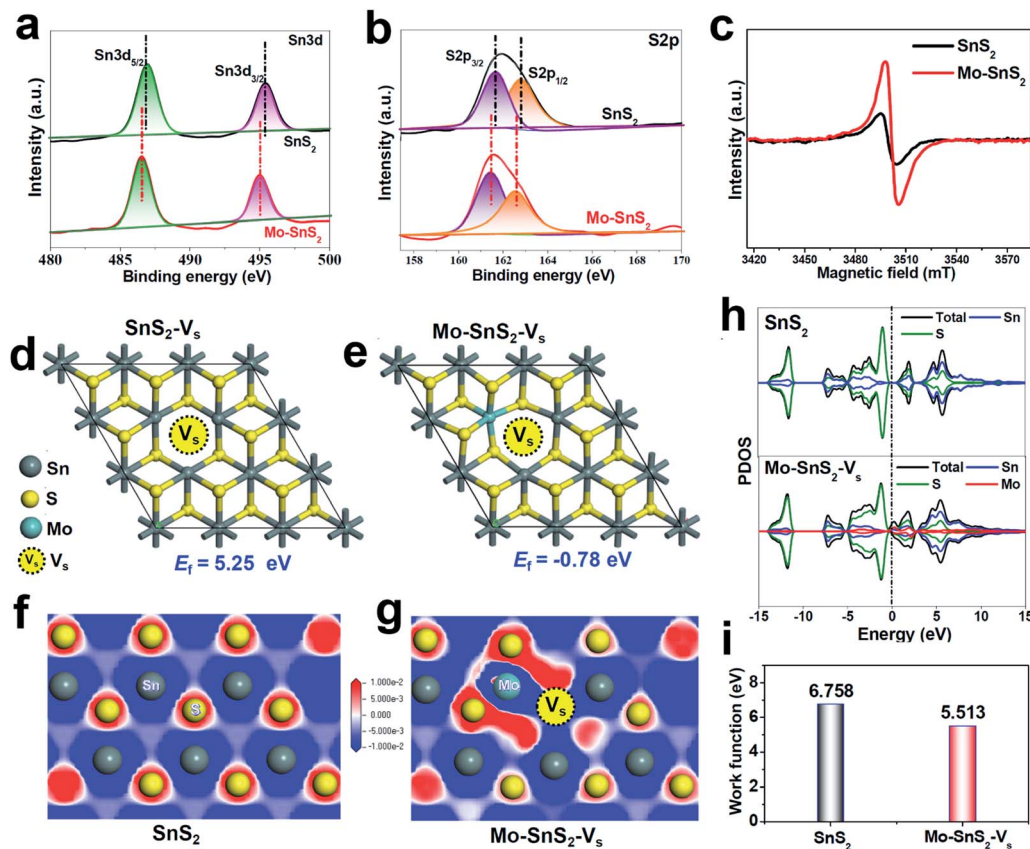
This journal is © The Royal Society of Chemistry 2020

J. Mater. Chem. A, 2020, **8**, 7117–7124 | 7119

Fig. 2 (a and b) XPS spectra of SnS_2 and $Mo\text{-}SnS_2$ nanosheets: (a) Sn3d and (b) S2p. (c) EPR spectra of SnS_2 and $Mo\text{-}SnS_2$ nanosheets. (d and e) Optimized SnS_2 structures with isolated V_s ($SnS_2\text{-}V_s$) and Mo-adjacent V_s ($Mo\text{-}SnS_2\text{-}V_s$), and the corresponding formation energies (E_f). (f and g) Electron contour maps of the (001) slice for (f) SnS_2 and (g) $Mo\text{-}SnS_2\text{-}V_s$. The blue and red regions represent electron depletion and accumulation, respectively. (h) PDOS of SnS_2 and $Mo\text{-}SnS_2\text{-}V_s$. (i) Calculated work functions of SnS_2 and $Mo\text{-}SnS_2\text{-}V_s$ (Fig. S2†).

close to the 1.15 µg mL^{-1} attained by the indophenol blue method with a reasonable margin of experimental error. Therefore, all these control experiments convincingly demonstrate that the produced NH_3 originates from the NRR.

The NRR performance of $Mo\text{-}SnS_2$/CC was then quantitatively examined by the combination of chronoamperometry testing with each cycle for 2 h of electrolysis (Fig. 3d) and UV-vis analysis (average of three measurements) at various potentials. The corresponding data of NH_3 yield and FE are shown in Fig. 3e. As observed, the NRR activity of $Mo\text{-}SnS_2$/CC exhibits optimum NRR performance with an NH_3 yield of 41.3 µg h^{-1} mg^{-1} at −0.5 V and a faradaic efficiency of 20.8% at −0.4 V. As shown in Table S1,† $Mo\text{-}SnS_2$/CC is the best SnS_2-based NRR catalyst reported to date and compares favorably to most state-of-the-art NRR catalysts. Nonetheless, the NRR performance shows a sharp decline at more negative potentials, which is attributed to the significantly enhanced HER.[57]

We also assessed the NRR performance of undoped SnS_2/CC for comparison under identical conditions. As shown in Fig. 3f, SnS_2/CC possesses a more inferior NRR activity with the highest NH_3 yield of 10.6 µg h^{-1} mg^{-1} at −0.5 V, which is about one-quarter that of $Mo\text{-}SnS_2$/CC (41.3 µg h^{-1} mg^{-1}), demonstrating that Mo-doping is able to dramatically promote the NRR activity of SnS_2 nanosheets. To elucidate the NRR

enhancement observed in $Mo\text{-}SnS_2$/CC, we determined the electrochemically active surface area (ECSA) by measuring the double-layer capacitance (C_{dl}). As shown in Fig. S11,† $Mo\text{-}SnS_2$/CC exhibits only a 1.3 times higher C_{dl}, but a ∼3.9 times higher NH_3 yield than SnS_2/CC, suggesting that the ECSA is not the primary factor and $Mo\text{-}SnS_2$/CC is intrinsically more active than SnS_2/CC. In addition, as depicted in the electrochemical impedance spectra (EIS, Fig. S12†), $Mo\text{-}SnS_2$/CC delivers a smaller charge-transport resistance than SnS_2/CC, indicating faster electron-transfer and enhanced NRR reaction kinetics of $Mo\text{-}SnS_2$/CC. This can be attributed to the synergistic role of the Mo-dopant and V_s in improving the conductivity of $Mo\text{-}SnS_2$, as revealed by the DFT results (Fig. 2h). Therefore, the combined Mo-dopant and V_s can bring about an improved conductivity and elevated intrinsic NRR activity, resulting in significantly enhanced NRR performance of $Mo\text{-}SnS_2$/CC.

We further evaluate the NRR stability which is another critical factor for practical applications.[58,59] Chronopotentiometric response measurements (Fig. 3g) reveal that the current density over $Mo\text{-}SnS_2$/CC presents a negligible degeneration for at least 20 h of continuous electrolysis, verifying the excellent long-term stability. Besides, when conducting seven chronoamperometric runs for $Mo\text{-}SnS_2$/CC, there is no remarkable change in the UV-vis spectra of the resultant electrolytes (Fig. S13†), nor in the
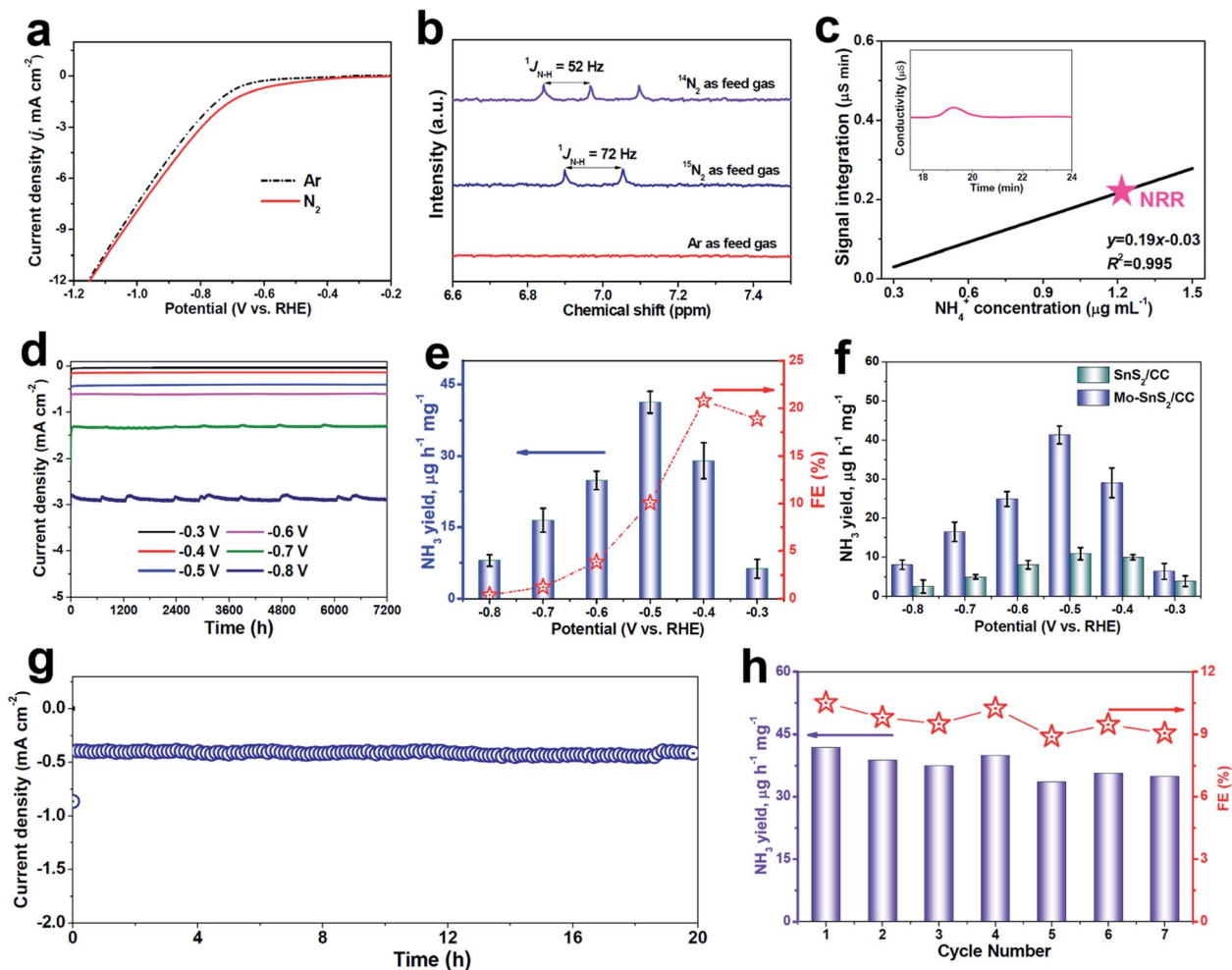
7120 | J. Mater. Chem. A, 2020, **8**, 7117–7124

This journal is © The Royal Society of Chemistry 2020

Fig. 3 (a) LSV curves of Mo-SnS$_2$/CC in Ar- and N$_2$-saturated solutions. (b) ^{1}H NMR spectra of electrolytes after NRR electrolysis for 2 h on Mo-SnS$_2$/CC using ^{14}N$_2$, ^{15}N$_2$ or Ar as feed gases. (c) IC spectra of the electrolyte after NRR electrolysis on Mo-SnS$_2$/CC for 2 h at −0.5 V (inset), and the determined NH$_4^+$ concentration of the electrolyte by referring to the calibration curve (Fig. S10†). (d) Chronoamperometry test results of Mo-SnS$_2$/CC for 2 h of NRR electrolysis at various potentials, and (e) the corresponding NH$_3$ yields and FEs. (f) NH$_3$ yields of SnS$_2$/CC and Mo-SnS$_2$/CC at various potentials. (g) Chronoamperometry test results of Mo-SnS$_2$/CC for 20 h of NRR electrolysis. (h) NH$_3$ yields and FEs of Mo-SnS$_2$/CC for seven cycles (each for 2 h of electrolysis at −0.5 V).

resulting NH$_3$ yield and FE data (Fig. 3h), confirming the good cycling stability. Further, the morphology, crystal phase and chemical bonding states of Mo-SnS$_2$ nanosheets can be well preserved after the stability test, as evidenced by SEM/TEM (Fig. S14†), XRD (Fig. S15†) and XPS (Fig. S16†) measurements. The outstanding stability of Mo-SnS$_2$/CC is believed to originate from the strong atomic and electronic bonding of Mo-dopants, 2D confinement effect of the nanosheet structure,[29] and direct nanosheet growth on CC with tight catalyst attachment.[31] Therefore, Mo-SnS$_2$/CC has great potential as a promising catalyst for electroreduction of N$_2$ to NH$_3$ with a favorable NH$_3$ production rate and robust stability.

DFT calculations based on the energetically stable Mo-SnS$_2$-V$_s$ structure (Fig. 2e) were further performed to gain deep insights into the synergistic role of the Mo-dopant and V$_s$ in facilitating the NRR. In view of N$_2$ adsorption as the critical step to initialize the NRR, N$_2$ adsorption behaviors over pristine SnS$_2$ and Mo-SnS$_2$-V$_s$ were first analyzed. For pristine SnS$_2$ (Fig. 4a

and b), the N$_2$ molecule barely adsorbs on either the central Sn site (Fig. 4a) or the edge Sn site (Fig. 4b), as evidenced by the negligible charge transfer and much less N≡N bond elongation (1.105 Å for the original N$_2$ gas), suggesting that pristine SnS$_2$ is almost inactive for the NRR. In sharp contrast, after N$_2$ adsorption on the V$_s$ site of Mo-SnS$_2$-V$_s$ (Fig. 4c), the N≡N bond is considerably elongated to 1.211 Å and 0.55$|e|$ is injected into *N$_2$, implying the greatly enhanced N$_2$ adsorption on Mo-SnS$_2$-V$_s$. The enlarged view (Fig. 4d) reveals a unique N$_2$ adsorption mode on the V$_s$ site of Mo-SnS$_2$-V$_s$, that is, the N$_2$ molecule is fixed to the Mo–Sn–Sn trimer center *via* a side-on configuration. Meanwhile, the N≡N triple bond is even cleaved to the N=N double bond without hydrogenation, indicating that the Mo–Sn–Sn trimer can strongly activate N$_2$ through an analogous dissociative pattern. As shown in the PDOS of the Mo–Sn–Sn trimer after N$_2$ adsorption (Fig. 4e), the Mo4d and Sn5p orbitals are both considerably hybridized with the N2p orbitals both below and above the Fermi level, suggesting the efficient back-
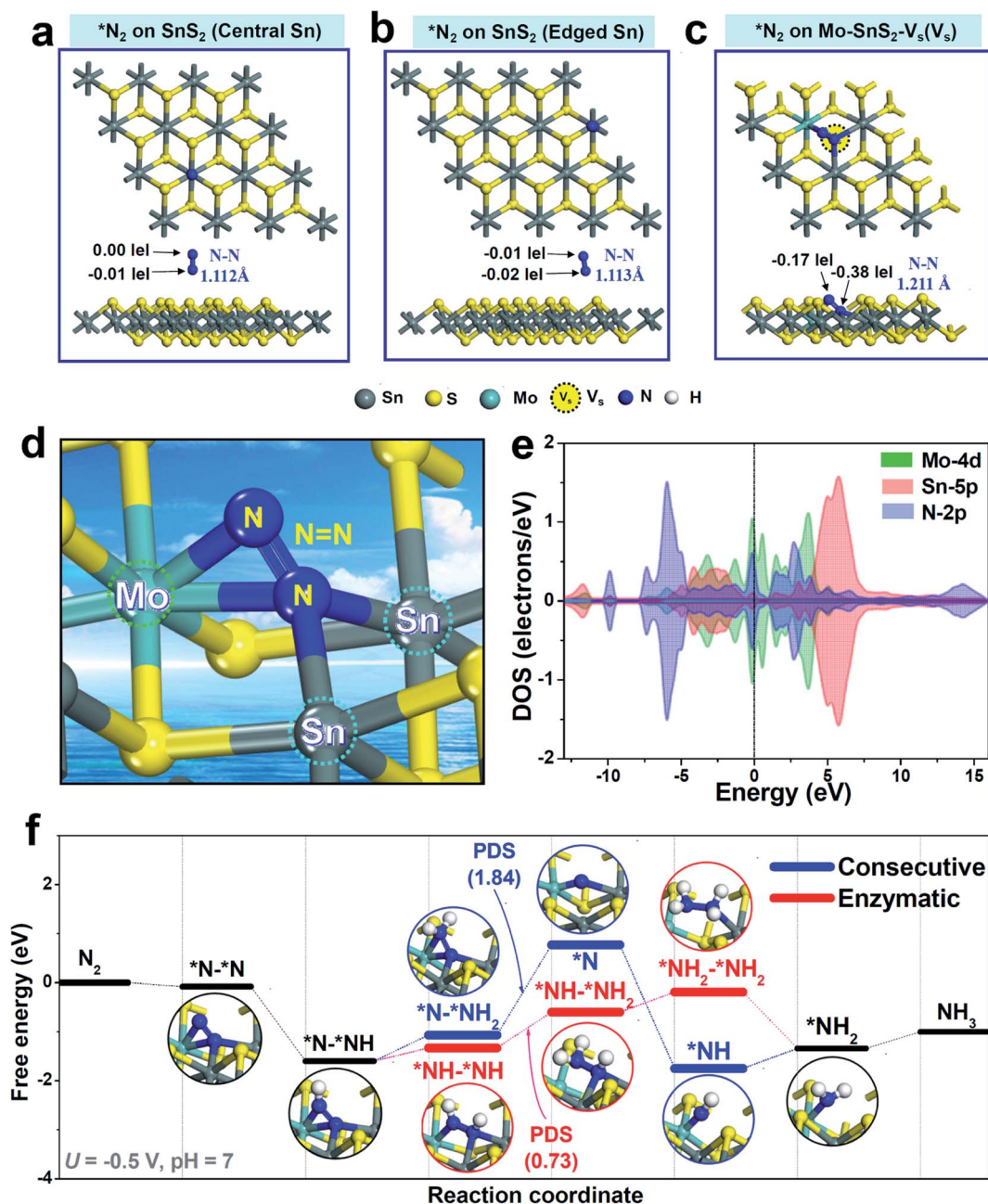
Fig. 4 (a–c) Optimized structures of N_2 adsorption on (a) SnS_2 (central Sn site), (b) SnS_2 (edge Sn site) and (c) Mo-SnS_2-V_s (V_s site). (d) Enlarged view of the N_2 adsorption mode on a V_s site of Mo-SnS_2-V_s (Mo–Sn–Sn trimer). (e) PDOS of the Mo–Sn–Sn trimer after N_2 adsorption. (f) Free energy diagrams of NRR consecutive/enzymatic reaction pathways over the Mo–Sn–Sn trimer at $U = -0.5$ V, pH = 7.

donation of electrons from the Mo–Sn–Sn trimer to $*N_2$.[60,61] The prominent back-donation of electrons from the Mo–Sn–Sn trimer to $*N_2$ can be directly visualized from the differential charge density (Fig. S17†), showing the pronouncedly accumulated electrons on $*N_2$. Mulliken charge analysis (Fig. S18†) reveals that the Mo–Sn–Sn trimer back-donates a total of $0.55|e|$ to $*N_2$, with $0.37|e|$ from the Mo dopant and $0.09|e|$ from each of the two Sn atoms. Hence, the co-presence of the Mo dopant and V_s in Mo-SnS_2-V_s enables the creation of Mo–Sn–Sn trimer catalytic sites that can strongly activate the N_2 molecule even for the cleavage of the N≡N triple bond to the N=N double bond at the N_2 adsorption stage.

The hydrogenation pathway of Mo-SnS_2-V_s was then evaluated using Gibbs free energy profiles through the consecutive (analogous to the distal pathway but *via* side-on configuration[62]) and enzymatic associative mechanisms, as shown in Fig. 4f. Optimized structures of all the NRR intermediates are presented in Fig. S19† (consecutive) and Fig. S20† (enzymatic). Notably, with the strong N_2 activation by the Mo–Sn–Sn trimer, the free energy of $*N–*NH$ even becomes negative, making the first hydrogenation step ($*N_2 \rightarrow *N–*NH$) occur spontaneously. This is in stark contrast to the largely positive free energy of $*N–NH$ (2.19 eV) observed in pristine SnS_2,[22] which has the first hydrogenation step ($*N_2 \rightarrow *N–NH$) as the potential

determining step (PDS). After the first hydrogenation, *N–*NH can be further hydrogenated through a consecutive or enzymatic pathway. For the consecutive pathway, *N–*NH$_2$ → *N is the PDS with a high energy barrier of 1.84 eV, while the PDS energy barrier (*NH–*NH → *NH–*NH$_2$) is substantially reduced to 0.73 eV for the enzymatic pathway. Hence, the hydrogenation of Mo-SnS$_2$-V$_s$ prefers to proceed via the enzymatic pathway with an overpotential of 0.57 V,[63] which is theoretically lower than that of most reported NRR catalysts.[64–67] These results demonstrate that the highly active Mo–Sn–Sn trimer provides Mo-SnS$_2$-V$_s$ with the downhill process of the first hydrogenation step, leading to the significantly decreased energy barrier and largely enhanced NRR activity.

On the other hand, as reported in the literature,[68,69] the surface charge and hydrogen bonding can affect the electrocatalytic calculations. As shown in Fig. S21,† after considering the effects of surface charge (adding one charge e$^-$ in the catalyst system) and hydrogen bonding (adding two H$_2$O molecules on the catalyst surface), we find that these two factors can make the free energies of *N$_2$ and *N–*NH become more negative but the downhill trend of the *N$_2$ → *N–*NH process still remains. Therefore, our main conclusion is not affected by the effects of surface charge and hydrogen bonding.

In conclusion, through combined experimental and theoretical investigations, we demonstrated that the synergistic modulation of vacancy engineering and heteroatom doping has been successfully achieved in Mo-SnS$_2$ nanosheets with enriched V$_s$, which showed greatly enhanced NRR performance with an NH$_3$ yield of 41.3 μg h^{-1} mg^{-1} (−0.5 V) and an FE of 20.8% (−0.4 V). DFT calculations revealed the unique NRR mechanism of Mo-SnS$_2$-V$_s$, in which the created Mo–Sn–Sn trimer active sites could strongly activate N$_2$ for even the cleavage of the N≡N triple bond to the N=N double bond at the N$_2$ adsorption stage, consequently resulting in a downhill process of the first hydrogenation step and a largely reduced energy barrier. This work not only offers an efficient strategy towards the design of SnS$_2$-based catalysts for highly efficient electrosynthesis of NH$_3$, but also provides new insights into the synergistic role of vacancies and dopants in regulating the NRR activity.

Conflicts of interest

There are no conflicts of interest to declare.

Acknowledgements

References

1 J. A. Brandes, N. Z. Boctor, G. D. Cody, B. A. Cooper, R. M. Hazen and H. S. Yoder Jr, *Nature*, 1998, **395**, 365.

2 X. Zhu, S. Mou, Q. Peng, Q. Liu, Y. Luo, G. Chen, S. Gao and X. Sun, *J. Mater. Chem. A*, 2020, **8**, 1545–1556.

3 G. F. Chen, S. Y. Ren, L. L. Zhang, H. Cheng, Y. R. Luo, K. H. Zhu, L. X. Ding and H. H. Wang, *Small Methods*, 2019, **3**, 1800337.

4 S. J. Li, D. Bao, M. M. Shi, B. R. Wulan, J. M. Yan and Q. Jiang, *Adv. Mater.*, 2017, **29**, 1700001.

5 H. Xie, Q. Geng, X. Zhu, Y. Luo, L. Chang, X. Niu, X. Shi, A. M. Asiri, S. Gao, Z. Wang and X. Sun, *J. Mater. Chem. A*, 2019, **7**, 24760–24764.

6 R. Zhao, C. Liu, X. Zhang, X. Zhu, P. Wei, L. Ji, Y. Guo, S. Gao, Y. Luo, Z. Wang and X. Sun, *J. Mater. Chem. A*, 2020, **8**, 77–81.

7 G. Deng, T. Wang, A. A. Alshehri, K. A. Alzahrani, Y. Wang, H. Ye, Y. Luo and X. Sun, *J. Mater. Chem. A*, 2019, **7**, 21674–21677.

8 H. Xian, Q. Wang, G. Yu, H. Wang, Y. Li, Y. Wang and T. Li, *Appl. Catal., A*, 2019, **581**, 116–122.

9 G. Yu, H. Guo, S. Liu, L. Chen, A. A. Alshehri, K. A. Alzahrani, F. Hao and T. Li, *ACS Appl. Mater. Interfaces*, 2019, **11**, 35764–35769.

10 H. Xian, H. Guo, Z. Chen, G. Yu, A. A. Alshehri, K. A. Alzahrani, F. Hao, R. Song and T. Li, *ACS Appl. Mater. Interfaces*, 2020, **12**, 2445–2451.

11 Y. R. Luo, G. F. Chen, L. Ding, X. Z. Chen, L. X. Ding and H. H. Wang, *Joule*, 2019, **3**, 279–289.

12 H. Cheng, L. X. Ding, G. F. Chen, L. L. Zhang, J. Xue and H. H. Wang, *Adv. Mater.*, 2018, **30**, 1803694.

13 K. Chu, Q. Q. Li, Y. H. Cheng and Y. P. Liu, *ACS Appl. Mater. Interfaces*, 2020, **12**, 11789–11796.

14 H. Cheng, P. X. Cui, F. R. Wang, L. X. Ding and H. H. Wang, *Angew. Chem., Int. Ed.*, 2019, **58**, 15541–15547.

15 X. Zhu, T. Wu, L. Ji, C. Li, T. Wang, S. Wen, S. Gao, X. Shi, Y. Luo, Q. Peng and X. Sun, *J. Mater. Chem. A*, 2019, **7**, 16117–16121.

16 L. Xia, X. Wu, Y. Wang, Z. Niu, Q. Liu, T. Li, X. Shi, A. M. Asiri and X. Sun, *Small Methods*, 2018, **3**, 1800251.

17 K. Chu, Q. Li, Y. Liu, J. Wang and Y. Cheng, *Appl. Catal., B*, 2020, **267**, 118693.

18 L. L. Zhang, L. X. Ding, G. F. Chen, X. F. Yang and H. H. Wang, *Angew. Chem., Int. Ed.*, 2019, **131**, 2638–2642.

19 L. Xia, J. Yang, H. Wang, R. Zhao, H. Chen, W. Fang, A. M. Asiri, F. Xie, G. Cui and X. Sun, *Chem. Commun.*, 2019, **55**, 3371–3374.

20 F. Li, L. Chen, G. P. Knowles, D. R. MacFarlane and J. Zhang, *Angew. Chem., Int. Ed.*, 2017, **56**, 505–509.

21 P. Li, W. Fu, P. Zhuang, Y. Cao, C. Tang, A. B. Watson, P. Dong, J. Shen and M. Ye, *Small*, 2019, **15**, 1902535.

22 X. Chen, Y.-T. Liu, C. Ma, J. Yu and B. Ding, *J. Mater. Chem. A*, 2019, **7**, 22235–22241.

23 Y. B. Li, Y. P. Liu, J. Wang, Y. L. Guo and K. Chu, *Inorg. Chem. Front.*, 2020, **7**, 455–463.

24 L. Yang, T. Wu, R. Zhang, H. Zhou, L. Xia, X. Shi, H. Zheng, Y. Zhang and X. Sun, *Nanoscale*, 2019, **11**, 1555–1562.

25 Z. Sun, R. Huo, C. Choi, S. Hong, T.-S. Wu, J. Qiu, C. Yan, Z. Han, Y. Liu, Y.-L. Soo and Y. Jung, *Nano Energy*, 2019, **62**, 869–875.

This journal is © The Royal Society of Chemistry 2020

J. Mater. Chem. A, 2020, **8**, 7117–7124 | 7123

26 L. Zhang, X.-Y. Xie, H. Wang, L. Ji, Y. Zhang, H. Chen, T. Li, Y. Luo, G. Cui and X. Sun, *Chem. Commun.*, 2019, **55**, 4627–4630.

27 C. Lv, Y. Qian, C. Yan, Y. Ding, Y. Liu, G. Chen and G. Yu, *Angew. Chem., Int. Ed.*, 2018, **57**, 10246–10250.

28 X. Yang, J. Nash, J. Anibal, M. Dunwell, S. Kattel, E. Stavitski, K. Attenkofer, J. G. Chen, Y. Yan and B. Xu, *J. Am. Chem. Soc.*, 2018, **140**, 13387–13391.

29 H. Jin, L. Li, X. Liu, C. Tang, W. Xu, S. Chen, L. Song, Y. Zheng and S.-Z. Qiao, *Adv. Mater.*, 2019, **31**, 1902709.

30 X. H. Wang, J. Wang, Y. B. Li and K. Chu, *ChemCatChem*, 2019, **11**, 4529–4536.

31 Y. P. Liu, Y. B. Li, H. Zhang and K. Chu, *Inorg. Chem.*, 2019, **58**, 10424–10431.

32 K. Chu, Y. Liu, Y. Chen and Q. Li, *J. Mater. Chem. A*, 2020, **8**, 5200–5208.

33 K. Chu, Y. H. Chen, Q. Q. Li, Y. P. Liu and Y. Tian, *J. Mater. Chem. A*, 2020, **8**, 5865–5873.

34 T. Wu, W. Kong, Y. Zhang, Z. Xing, J. Zhao, T. Wang, X. Shi, Y. Luo and X. Sun, *Small Methods*, 2019, 1900356.

35 C. Guo, X. Liu, L. Gao, X. Kuang, X. Ren, X. Ma, M. Zhao, H. Yang, X. Sun and Q. Wei, *Appl. Catal., B*, 2020, **263**, 118296.

36 K. Chu, Y. P. Liu, Y. B. Li, Y. L. Guo, Y. Tian and H. Zhang, *Appl. Catal., B*, 2020, **264**, 118525.

37 T. Wu, Z. Xing, S. Mou, C. Li, Y. Qiao, Q. Liu, X. Zhu, Y. Luo, X. Shi, Y. Zhang and X. Sun, *Angew. Chem., Int. Ed.*, 2019, **58**, 18449–18453.

38 N. Cao, Z. Chen, K. Zang, J. Xu, J. Zhong, J. Luo, X. Xu and G. Zheng, *Nat. Commun.*, 2019, **10**, 1–12.

39 K. Chu, X. H. Wang, Y. B. Li, D. J. Huang, Z. R. Geng, X. L. Zhao, H. Liu and H. Zhang, *Mater. Des.*, 2018, **140**, 85–94.

40 K. Chu, J. Wang, Y. P. Liu and Z. R. Geng, *Carbon*, 2018, **140**, 112–123.

41 K. Chu, X. H. Wang, F. Wang, Y. B. Li, D. J. Huang, H. Liu, W. L. Ma, F. X. Liu and H. Zhang, *Carbon*, 2018, **127**, 102–112.

42 K. Chu, J. Wang, Y. P. Liu, Y. B. Li, C. C. Jia and H. Zhang, *Carbon*, 2019, **143**, 85–96.

43 K. Chu, F. Wang, X. H. Wang, Y. B. Li, Z. R. Geng, D. J. Huang and H. Zhang, *Mater. Des.*, 2018, **144**, 290–303.

44 K. Chu, F. Wang, Y. B. Li, X. H. Wang, D. J. Huang and H. Zhang, *Carbon*, 2018, **133**, 127–139.

45 L. Meng, S. Wang, F. Cao, W. Tian, R. Long and L. Li, *Angew. Chem., Int. Ed.*, 2019, **58**, 6761–6765.

46 M.-A. Légaré, G. Bélanger-Chabot, R. D. Dewhurst, E. Welz, I. Krummenacher, B. Engels and H. Braunschweig, *Science*, 2018, **359**, 896–900.

47 J. Wang, Y. P. Liu, H. Zhang, D. J. Huang and K. Chu, *Catal. Sci. Technol.*, 2019, **9**, 4248–4254.

48 Y. P. Liu, Y. B. Li, D. J. Huang, H. Zhang and K. Chu, *Chem.–Eur. J.*, 2019, **25**, 11933–11939.

49 K. Chu, Y. P. Liu, Y. B. Li, J. Wang and H. Zhang, *ACS Appl. Mater. Interfaces*, 2019, **11**, 31806–31815.

50 L. Li, C. Tang, B. Xia, H. Jin, Y. Zheng and S.-Z. Qiao, *ACS Catal.*, 2019, **9**, 2902–2908.

51 D. Zhu, L. Zhang, R. E. Ruther and R. J. Hamers, *Nat. Mater.*, 2013, **12**, 836.

52 G. W. Watt and J. D. Chrisp, *Anal. Chem.*, 1952, **24**, 2006–2008.

53 K. Chu, Y. P. Liu, Y. B. Li, Y. L. Guo and Y. Tian, *ACS Appl. Mater. Interfaces*, 2020, **12**, 7081–7090.

54 J. Yu, C. Li, B. Li, X. Zhu, R. Zhang, L. Ji, D. Tang, A. M. Asiri, X. Sun, Q. Li, S. Liu and Y. Luo, *Chem. Commun.*, 2019, **55**, 6401–6404.

55 R. Zhang, L. Ji, W. Kong, H. Wang, R. Zhao, H. Chen, T. Li, B. Li, Y. Luo and X. Sun, *Chem. Commun.*, 2019, **55**, 5263–5266.

56 C. Li, J. Yu, L. Yang, J. Zhao, W. Kong, T. Wang, A. M. Asiri, Q. Li and X. Sun, *Inorg. Chem.*, 2019, **58**, 9597–9601.

57 A. R. Singh, B. A. Rohr, J. A. Schwalbe, M. Cargnello, K. Chan, T. F. Jaramillo, I. Chorkendorff and J. K. Norskov, *ACS Catal.*, 2016, **7**, 706–709.

58 P. Wang, Q. Q. Li, Y. H. Cheng and K. Chu, *J. Mater. Sci.*, 2020, **55**, 4624–4632.

59 F. Wang, Y. P. Liu, H. Zhang and K. Chu, *ChemCatChem*, 2019, **11**, 1441–1447.

60 Q. Li, L. He, C. Sun and X. Zhang, *J. Phys. Chem. C*, 2017, **121**, 27563–27568.

61 Y.-C. Hao, Y. Guo, L.-W. Chen, M. Shu, X.-Y. Wang, T.-A. Bu, W.-Y. Gao, N. Zhang, X. Su, X. Feng, J.-W. Zhou, B. Wang, C.-W. Hu, A.-X. Yin, R. Si, Y.-W. Zhang and C.-H. Yan, *Nat. Catal.*, 2019, **2**, 448–456.

62 L. Shi, Q. Li, C. Ling, Y. Zhang, Y. Ouyang, X. Bai and J. Wang, *J. Mater. Chem. A*, 2019, **7**, 4865–4871.

63 J. Zhao and Z. Chen, *J. Am. Chem. Soc.*, 2017, **139**, 12480–12487.

64 K. Chu, Y. Liu, J. Wang and H. Zhang, *ACS Appl. Energy Mater.*, 2019, **2**, 2288–2295.

65 K. Chu, Y. Liu, Y. Li, H. Zhang and Y. Tian, *J. Mater. Chem. A*, 2019, **7**, 4389–4394.

66 Z. Wang, F. Gong, L. Zhang, R. Wang, L. Ji, Q. Liu, Y. Luo, H. Guo, Y. Li, P. Gao, X. Shi, B. Li, B. Tang and X. Sun, *Adv. Sci.*, 2018, 1801182.

67 X. Li, T. Li, Y. Ma, Q. Wei, W. Qiu, H. Guo, X. Shi, P. Zhang, A. M. Asiri, L. Chen, B. Tang and X. Sun, *Adv. Energy Mater.*, 2018, **8**, 1801357.

68 X. Zhao and Y. Liu, *J. Am. Chem. Soc.*, 2020, **142**, 5773–5777.

69 D. Kim, J. Shi and Y. Liu, *J. Am. Chem. Soc.*, 2018, **140**, 9127–9131.

7124 | *J. Mater. Chem. A*, 2020, **8**, 7117–7124

This journal is © The Royal Society of Chemistry 2020